Tungsten (2021) 3:470–481
https://doi.org/10.1007/s42864-021-00110-9

Tungsten
www.springer.com/42864

ORIGINAL PAPER

Check for updates

Transmission electron microscopy characterization of dislocation loops in irradiated zirconium

Si-Mian Liu[1] · **Wei-Zhong Han**[1]

Received: 23 April 2021 / Revised: 26 May 2021 / Accepted: 27 May 2021 / Published online: 4 August 2021

Abstract

Characterization of irradiation defects is of great importanceto mitigate irradiation damage, reduce irradiation growth and tune mechanical properties in Zr alloys. Here, we describe a practical method to characterize the dislocation loops in irradiated Zr using conventional transmission electron microscopy (TEM). Vacancy or interstitial nature of dislocation loops is determined using the inside and outside contrast method. The habit plane of dislocation loops is determined by tilting the sample to multiple zone axes and judged based on the projected loop shape. The size of $\langle a \rangle$ loops is measured by tilting the sample to an edge-on position and the loop number is counted under a weak-beam dark-field TEM condition. $\langle c \rangle$ loops have a line contrast under viewing direction of *a*-axis and a circular shape under viewing direction of *c*-axis. In addition, a large number of triangle-shaped vacancy platelets (TVPs) were formed on the basal plane. With increasing the irradiation damage from 0.5 to 1.5 dpa, the number density of $\langle a \rangle$ loops keeps constant, while the number density of TVPs increased significantly, owing to the anisotropic diffusion and accumulation of point defects within basal plane. The methods introduced here are easy to follow and extend into other related investigations.

Keywords Irradiation damage · Dislocation loop · Habit plane · Zirconium alloys

1 Introduction

Zirconium (Zr) and its alloys are widely used as cladding tubes and structural materials in nuclear reactors. The degradation of mechanical properties and damage after irradiation have a strong relationship with the generation of irradiation defects. Dislocation loops of $\langle a \rangle$ and $\langle c \rangle$ types are well known as the main defect structures in Zr after high energy particle irradiation [1–14]. The $\langle a \rangle$ loops, no matter interstitial or vacancy type, were found forming on the primary and secondary prismatic plane with the same Burgers vector $1/3\langle 11\bar{2}0 \rangle$ [1, 4]. The $\langle c \rangle$ loops are always in vacancy type, formed on the basal plane with Burgers vector $1/6\langle 2\bar{2}03 \rangle$ or 1/2[0001] [15].

The anisotropic irradiation growth of cladding tubes is a common issue in nuclear reactor. Irradiation growth shows three stages characteristics, stage I—initial transient with rapid irradiation growth, stage II—steady-state with a constant growth strain and stage III—breakthrough growth with high growth rate [16]. The various stages are related to the evolution and distribution of irradiation defects, such as $\langle a \rangle$ and $\langle c \rangle$ dislocation loops [17, 18]. $\langle a \rangle$ type loops are generated in the first two stages, while $\langle c \rangle$ type loops are always observed after reaching a critical level of radiation damage at stage III [17–21].

The evolution of $\langle a \rangle$ loops as a function of irradiation dose in Zr alloys has been characterized [11, 20–24]. With the accumulation of point defects, the size of $\langle a \rangle$ type loops increases gradually. Sometimes the inverse trend was observed, which was attributed to the effect of alloy elements [20, 21]. The density of $\langle a \rangle$ dislocation loops rises at low dose and tends to reach a saturation after 0.2 displacement per atom (dpa) [15–19]. However, the relationship between the first two stages of irradiation growth and the characteristics of $\langle a \rangle$ loops was not well established. The change of the vacancy- and interstitial-type defects with enhancing irradiation dose has not been analyzed in detail. Therefore, the accumulation of point defects with increasing irradiation dose can be understood by analyzing the number density and nature of dislocation loops.

✉ Wei-Zhong Han
wzhanxjtu@mail.xjtu.edu.cn

[1] Center for Advancing Materials Performance from the Nanoscale, State Key Laboratory for Mechanical Behavior of Materials, Xi'an Jiaotong University, Xi'an 710049, China

Dislocation loops include both interstitial-type and vacancy-type, which are outcomes of the agglomerating of interstitials or vacancies. The nature of dislocation loops can be identified using transmission electron microscope (TEM). Techniques developed by "Groves and Kelly", "Edmondson and Williamson" and "Maher and Eyre" were used to determine the nature of the dislocation loops in early studies [25–27]. The inside and outside contrast method modified by Föll et al. [28] is more effective and widely used to analyze dislocation loops in past decades. In this method, four steps are required to determine the characteristics of a non-edge dislocation loop:

(i) Using conventional right-hand /finish-start (RH/FS) method or invisible criterion [26] $\vec{g}\cdot\vec{b}=0$ to determine the Burgers vector roughly.
(ii) Taking bright field images under a pair of diffraction vector "$+\vec{g}$" and "$-\vec{g}$" with strict kinematic two-beam imaging condition (deviation parameter $S_g>0$). According to the criterion that the loops show "outside" contrast with $(\vec{g}\cdot\vec{b})\cdot S_g>0$ and "inside" contrast with $(\vec{g}\cdot\vec{b})\cdot S_g<0$, the sign of Burgers vector is finalized.
(iii) Determining the habit plane of each dislocation loop.
(iv) Defining the nature of a loop by the angle between its Burgers vector and habit plane normal, which always points upwards toward the electron beam direction. For interstitial type, $\vec{b}\cdot\vec{n}>0$ and vacancy type, $\vec{b}\cdot\vec{n}<0$.

Only steps (i) and (ii) are needed for a pure-edge dislocation loop because outside contrast indicates an interstitial loop and inside contrast indicates a vacancy loop. The unsafe region, which has been given the different definition and described in stereographic projection is the primary problem when characterizing the non-edge dislocation loops [2, 9, 29, 30]. The unsafe region can be understood at some orientations, under which the habit plane of a dislocation loop cannot be determined accurately [4, 8]. It was proposed that 1/3 $\langle a\rangle$ loops were in an unsafe region when observing from the $[1\bar{2}13]$ zone axis [8]. It is difficult to determine the habit plane normal direction $\vec{n}$ of these loops from this zone axis because these $\langle a\rangle$ loops have an edge-on orientation so that the loop normal direction is perpendicular to the electron beam direction. However, if the habit plane and loop normal direction of all the loops are known, no safe or unsafe problem exists. Therefore, it is critical to determine the habit plane of the $\langle a\rangle$ dislocation loops.

With above four steps, it is still very difficult to determine the habit plane of the individual dislocation loop. Conventional two-surface trace analysis is a traditional way to determine the habit plane [9]. According to the trace of the major axis of the elliptical loop image plus the angle between the normal direction and electron beam direction, the habit plane of dislocation loops can be determined [9]. It was found that the $\langle a\rangle$ loops are lying on or near the prismatic plane. The best way is to tilt the $\langle a\rangle$ loops to an edge-on orientation and the loop plane normal direction $\vec{n}$ can be evaluated from the loop trace [8]. However, the requirement for the tilting range of the sample stage is a great challenge, especially when tilting it from the prismatic plane to the basal plane in a hexagonal close-packed (HCP) Zr.

Ion irradiation is an efficient way to replace neutron irradiation to study the defects in metals [12–14]. In this study, we take a helium-ion-irradiated Zr as a model system to show how to determine the characteristics of dislocation loops, including Burgers vector, habit plane, interstitial or vacancy nature, loop size and number density. The evolution of irradiation defects with increasing irradiation damage and their consequence are further discussed. The methodology adopted in this study provide a good reference for other researchers in related field to analyze irradiation induced dislocation loops.

2 Experimental

Pure Zr (purity > 99.99%) samples were used as model materials, with specific orientation near $[1\bar{2}10]$ and [0001] zone axis. The material composition can be found in Table 1. The bulk sample was annealed at 800 °C for 2 h in a high vacuum atmosphere (~ 10^{-4} Pa) to remove the pre-existing defects. Thin foils for TEM were first mechanically ground to less than 50 μm in thickness and then twin-jet polished to electron transparency. Helium ion irradiation was conducted in a vacuum of ~10^{-5} Pa at 400 °C using a National Electrostatic Corporation (NEC) 400 kV ion implanter. The selected irradiation temperature is expected to obtain a conductive loop size for characterization under the TEM. The ion fluence ranged from 1×10^{17} ions·m^{-2} to 3×10^{17} ions·m^{-2} with an invariant dose rate of 1.67×10^{13} ions·m^{-2}·s^{-1}.

The irradiation damage and helium concentration were simulated by the Stopping and Ranges of Ions in Matter (SRIM) with full damage cascades mode and a displacement energy of 40 eV for Zr [31]. The irradiation damage and helium concentration profiles with different irradiation dose were plotted in Fig. 1. The average irradiation damage is about 0.5 dpa or 1.5 dpa for helium irradiation with fluence of 1×10^{17} ions·m^{-2} or 3×10^{17} ions·m^{-2}, respectively. The TEM foil was cut in half to conduct a thickness measurement inside a scanning electron microscopy (SEM). The sample thickness of TEM foils ranged

Table 1 Impurities of Zr sample (wt%)

Hf	Fe	Si	Sn	Ni	Cr	O	C
≤0.001	≤0.002	≤0.001	≤0.0005	≤0.0007	≤0.0008	≤0.014	≤0.001

from 60 to 200 nm. After irradiation, the helium concentration in the TEM foils is negligible. Radiation defects were characterized using a JEOL 2100F with a conventional TEM diffraction contrast technique. The irradiated side of the sample was placed facing down so that the irradiated surface can upwards to the electron beam due to the 180-degree inversion. The sample stage has a tilt angle range from $-30°$ to $+30°$ on both x and y axes. Bright field TEM images under different two-beam conditions were recorded to analyze the characteristics of dislocation loops.

3 Burgers vector of dislocation loop

In most cases, the invisible criterion $\vec{g}\cdot\vec{b}=0$ is used to determine the Burgers vector of the loops, requiring more than two diffraction vectors ($\vec{g}$) under different zone axes. Turning from one zone axis to another usually requires a tilting angle of more than 15°. To avoid the interference of stress field during this process, a flat region with good contrast is necessary. It is better to find a marker, such as a dislocation line, precipitate, grain boundary or interface, to guide and locate the dislocation loop during tilting operation. Otherwise, it is very easy to lose the targeted dislocation loops. Figure 2a shows $\langle a\rangle$ dislocation loops with three $\langle 2\bar{1}\bar{1}0\rangle$ Burgers vector when tilting the zone axis 0.5° away from $[4\bar{2}\bar{2}\bar{3}]$. The vector $\vec{g}=10\bar{1}1$, $\vec{g}=1\bar{1}01$ and $\vec{g}=01\bar{1}0$ under zone axis (ZA) $=[2\bar{1}\bar{1}0]$ were adopted to determine the Burgers vectors of the dislocation loops. The loops marked by green arrows show no contrast (Fig. 2b) under $\vec{g}=10\bar{1}1$, indicating that the loop Burgers vector is $\pm\frac{1}{3}[\bar{1}2\bar{1}0]$. The loops marked by yellow arrows have a Burgers vector of $\pm\frac{1}{3}[\bar{1}\bar{1}20]$ (Fig. 2c) and the loop marked by red arrows have a Burgers vector of $\pm\frac{1}{3}[\bar{1}\bar{1}20]$ (Fig. 2d). The tilting angle was shown in the schematic diagram and the a-direction was specified in Fig. 2e as well.

Figures 2d and 3a are two bright field images taken with a pair of $\vec{g}$ to determine the sign of the Burgers vector. Dislocation loops labeled with A and C show outside contrast while loops labeled B and A' show inside contrast with $\vec{g}=0\bar{1}10$ (Fig. 3a). This means A loops have a Burgers vector of $-\frac{1}{3}[\bar{1}\bar{1}20]$, B and A' loops have a Burgers vector of $\frac{1}{3}[\bar{1}\bar{1}20]$ and C loops have a Burgers vector of $-\frac{1}{3}[\bar{1}2\bar{1}0]$. These parameters are listed in Table 2 for comparison.

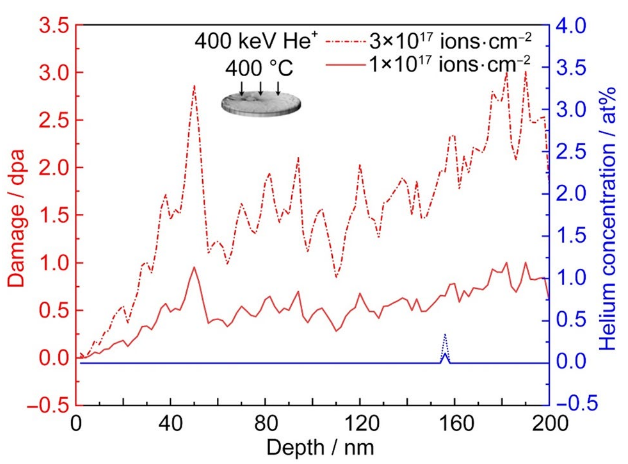

Fig. 1 Radiation damage (red curves) and helium concentration (blue curves) with depth in the thin foil Zr within 200 nm. The maximum radiation damage is less than 3 dpa for irradiation fluence of 3×10^{17} ions·cm^{-2} and 1 dpa for irradiation fluence of 1×10^{17} ions·cm^{-2}

4 Dislocation loop habit plane

Next, we introduce some tips to determine the habit plane of $\langle a\rangle$ loops. First, the non-edge prismatic $\langle a\rangle$ loops mean the Burgers vector cannot be parallel or perpendicular to the habit plane [8–10, 32]. For the A loops with $\vec{b}=-\frac{1}{3}[\bar{1}\bar{1}20]$ indicated by yellow arrows in Figs. 2c and 3, their habit planes are not parallel to the $(1\bar{1}00)$ nor $(\bar{1}\bar{1}20)$. Second, utilize the projected change of $\langle a\rangle$ loops to determine the loop plane. Figure 4 displays the morphology of $\langle a\rangle$ loops from various loop planes projecting on the $(10\bar{1}0)$ and $(2\bar{1}\bar{1}3)$. For the loops projecting on the $\{10\bar{1}0\}$, most of them have an elliptical shape with different aspect ratio (Fig. 4a). Here, we use the aspect ratio to describe the shape of an elliptical loop. If the axis aligned to the basal plane is represented by a and the axis aligned to the [0001] direction is represented by b, the aspect ratio of the loop projection is b'/a'. Figure 4b shows the loops lying on the $(01\bar{1}0)$ and $(1\bar{1}00)$ have the largest projection aspect ratio. Therefore, the elliptical loops with a large aspect ratio, indicated by the blue arrows in Fig. 4a, are on the $(01\bar{1}0)$ or $(1\bar{1}00)$ plane. The loops lying on the $(\bar{1}2\bar{1}0)$ can also be separated out, owing to their edge-on contrast (Fig. 4b). Different from the projection on the $(10\bar{1}0)$, the $\langle a\rangle$ loops projected on the $(2\bar{1}\bar{1}3)$ have a near circular shape, as indicated by green arrows in Fig. 4c. The loop in red arrow in Fig. 4c is on the $(01\bar{1}0)$, because only the loops on the $(01\bar{1}0)$ show a line contrast when observed from $[2\bar{1}\bar{1}3]$ (Fig. 4d).

When turning from $[2\bar{1}\bar{1}3]$ to $[2\bar{1}\bar{1}0]$, the A loops always show a coffee bean-like contrast and gradually becomes longer (means aspect ratio increasing), indicating they are lying on the $(0\bar{1}10)$ plane (Fig. 3a–d). Figure 3e shows the configuration of $\langle a\rangle$ loops projecting on the different planes by tilting the sample stage from $[2\bar{1}\bar{1}3]$ to $[10\bar{1}0]$, along the $(0\bar{1}10)$ and (0002) Kikuchi line with little change of deviation factor S_g. For B loops with $\vec{b}=-\frac{1}{3}[\bar{1}\bar{1}20]$, the contrast is near a circle during tilting process, which indicate that they are not belong to $(1\bar{1}00)$, $(0\bar{1}10)$, $(\bar{1}\bar{1}20)$ nor $(\bar{1}2\bar{1}0)$ planes. The aspect ratio of B loops becomes smaller when the stage

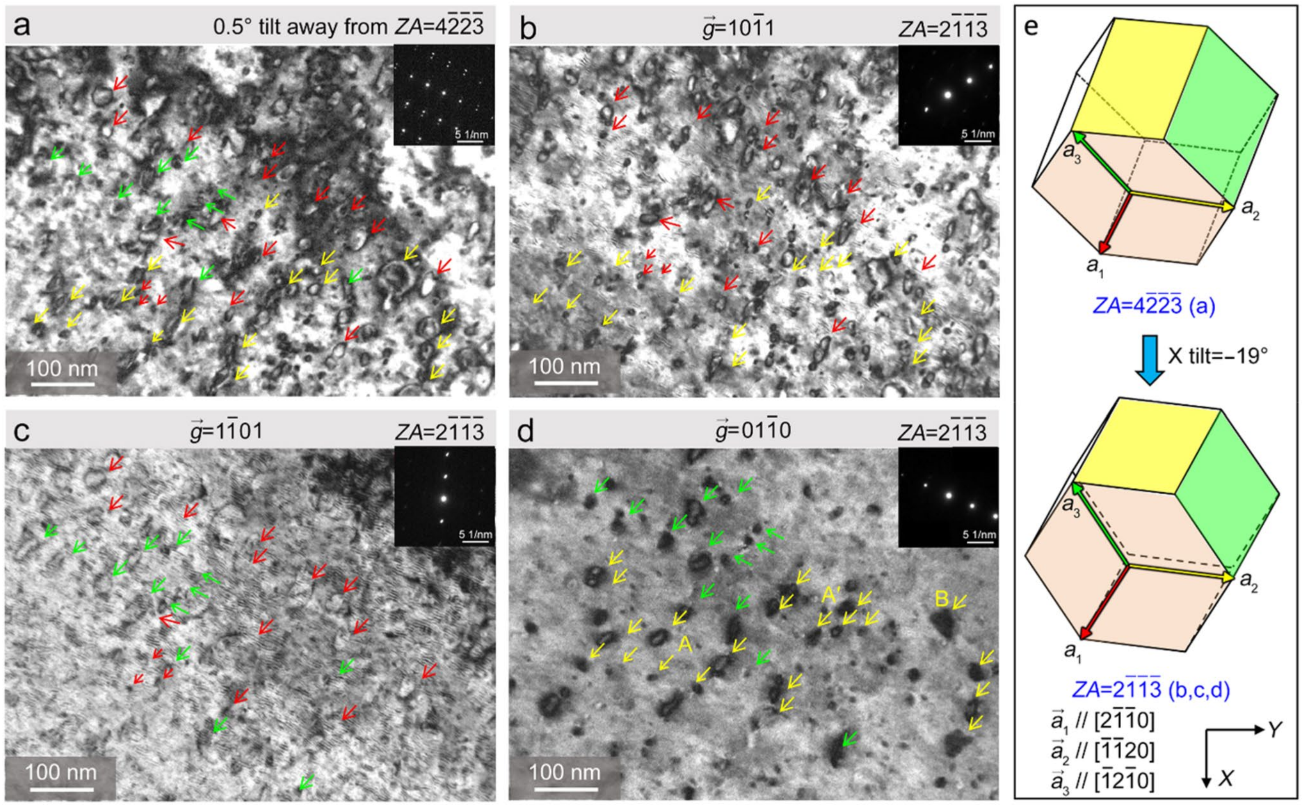

Fig. 2 Determination of the Burgers vector of ⟨a⟩ dislocation loops in pure Zr after helium irradiation to a fluence of 3×10^{17} ions·cm^{-2} at 400 °C. **a** All three types of ⟨a⟩ loops showing contrast under $[4\bar{2}\bar{2}\bar{3}]$ zone axis, as marked by the colored arrows. **b** Loop contrast with $\vec{g}=[10\bar{1}1]$ under $[2\bar{1}\bar{1}3]$ zone axis. **c** Loop contrast with $\vec{g}=[1\bar{1}01]$ under $[2\bar{1}\bar{1}3]$ zone axis. **d** Loop contrast with $\vec{g}=[01\bar{1}0]$ under $[2\bar{1}\bar{1}3]$ zone axis. **e** A schematic diagram showing the tilting angle between the $[4\bar{2}\bar{2}\bar{3}]$ and $[2\bar{1}\bar{1}3]$ zone axis

was tilted from $[2\bar{1}\bar{1}0]$ to $[10\bar{1}0]$. Therefore, the B loops are lying on the $\{2\bar{1}\bar{1}0\}$ instead of $(10\bar{1}0)$. Even though both A and B loops meet the same extinction conditions and have the same Burgers vector, they are not on the same habit plane. The habit planes of A and C loops can be determined using the same method and are listed in Table 2.

5 Dislocation loop nature

The direction of the plane normal $\vec{n}$ is upwards to the beam direction, whose relationship with the Burgers vector was drawn in Fig. 4a. Using $\vec{b}\cdot\vec{n}<0$, those *A'* loops with elliptical shape are vacancy-type, and since $\vec{b}\cdot\vec{n}>0$, *B* loops with near-circular shape are of interstitial type. We analyzed 126 dislocation loops, which are from different zones and under the same diffraction conditions. A total of 60 vacancy- and 66 interstitial-type loops were found in this region. The ratio of vacancy loops to the interstitial loops equals 1.1 for Zr foil with radiation damage of 1.5 dpa. The statistics have errors because dislocation loops with size less than 4 nm are difficult to be analyzed by the inside and outside method.

A similar operation was carried out near the $[10\bar{1}1]$ zone axis in Zr foil with 0.5 dpa in Fig. 5. The vectors $\vec{g}=[01\bar{1}\bar{1}]$ near the $[2\bar{1}\bar{1}0]$ zone axis and $\vec{g}=[\bar{1}101]$ and $\vec{g}=[1\bar{1}0\bar{1}]$ near the $[10\bar{1}1]$ zone axis are used to analyze the nature of the dislocation loops. After specifying the ⟨a⟩ type loops under $\vec{g}=[0002]$ with ZA $=[2\bar{1}\bar{1}0]$, the zone axis was tilt to the $[10\bar{1}1]$ zone axis along $(01\bar{1}\bar{1})$ Kikuchi line (Fig. 5e). The tilting angle and the procedures are illustrated in Fig. 5d, e. The loops labeled with arrows in red, yellow and green have three different $\langle 2\bar{1}\bar{1}0\rangle$ Burgers vectors, respectively. According to the aspect ratio of projection and Fig. 4, the plane normal of the dislocation loop was inferred and marked in Fig. 5d. The detailed analysis results are listed in Table 3. We analyzed 98 dislocation loops in the Zr foil with 0.5 dpa. The ratio of the vacancy loops to the interstitial loops is 55:33, which is approximately 1.3.

6 Size of dislocation loop

The loop size is another indicator to measure the radiation damage. The size distribution of ⟨a⟩ dislocation loops produced after different irradiation conditions is discrete

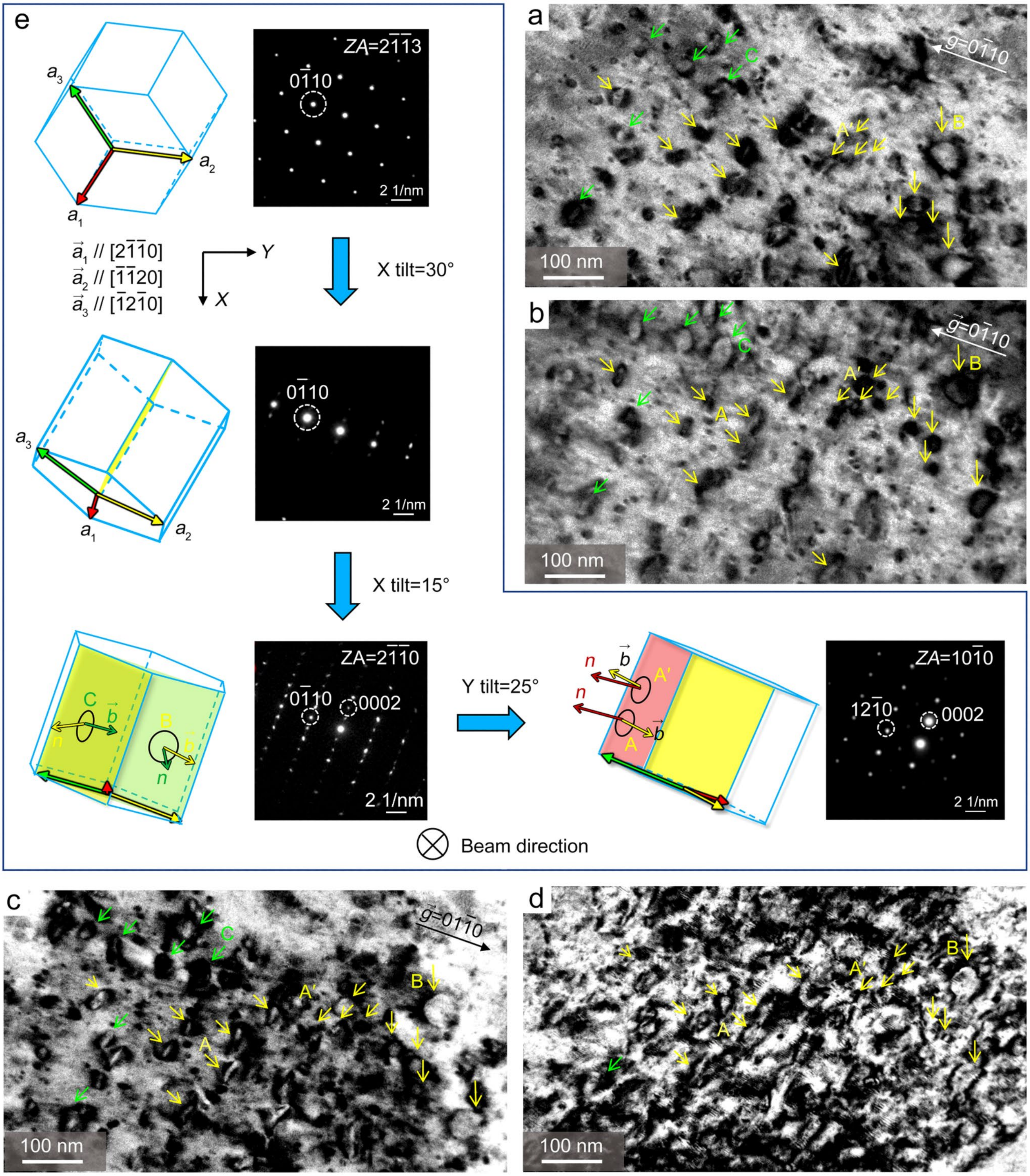

Fig. 3 Procedures of determining the habit plane of $\langle a \rangle$ loops via titling the sample to different crystallographic orientations. **a**–**d** Bright field TEM images of $\langle a \rangle$ loops with Burgers vectors of $\pm\frac{1}{3}[\bar{1}\bar{1}20]$ (yellow arrow) and $\pm\frac{1}{3}[\bar{1}2\bar{1}0]$ (green arrow). **e** Schematic of HCP model and its corresponding diffraction pattern under different viewing orientations. The direction of electron beam points inward. Relationship between the plane normal and Burgers vector of the A, A', B and C loops are labeled

[8–13, 20–24] because dislocation loops are measured via the projection of the dislocation loops on various planes, and most likely this size deviates from their real size. The accurate way to measure the loops is when the electron beam is parallel to the loop habit plane. But it is difficult to guarantee that all $\langle a \rangle$ loops lie on their habit plane under

Table 2 Characteristics of ⟨a⟩ dislocation loops formed under helium irradiation to 1.5 dpa in Figs. 2 and 3

Number	Contrast for $\vec{g} = 01\bar{1}0$	Burgers vector	Habit plane	Type in nature
A	Inside	$\frac{1}{3}[\bar{1}\bar{1}20]$	$01\bar{1}0$	Vacancy
A'	Outside	$-\frac{1}{3}[\bar{1}\bar{1}20]$	$01\bar{1}0$	Interstitial
B	Inside	$\frac{1}{3}[\bar{1}\bar{1}20]$	$2\bar{1}\bar{1}0$	Interstitial
C	Inside	$-\frac{1}{3}[\bar{1}2\bar{1}0]$	$1\bar{1}00$	Vacancy

a single zone axis. In this study, we selected the [0001] zone axis to measure the size of ⟨a⟩ loops (Fig. 6). From this orientation, all ⟨a⟩ loops with prismatic habit plane have an edge-on position and show a coffee bean-like contrast, as displayed in Fig. 6a. The colored arrows in Fig. 6a mark the loops on three different prismatic planes $\{10\bar{1}0\}$ according to the diffraction pattern in Fig. 6b. The loops marked with 1, 2 and 3 are on the planes between the $\{10\bar{1}0\}$ and $\{11\bar{2}0\}$, which deviate from the normal habit plane of ⟨a⟩ loops. Figure 6c shows the schematic diagram of different loops and their projection on the basal plane. A similar result was also found in the pure Zr with irradiation damage of 1.5 dpa (Fig. 6d, e). The pink and blue lines are projection of ⟨a⟩ loops lying on $\{10\bar{1}0\}$ and $\{11\bar{2}0\}$, respectively [1, 30]. Some calculations indicated that ⟨a⟩ loops prefer to rotate onto the secondary prismatic plane to reduce energy after forming on the primary prismatic plane [33]. Supposing that the ⟨a⟩ loops are all in

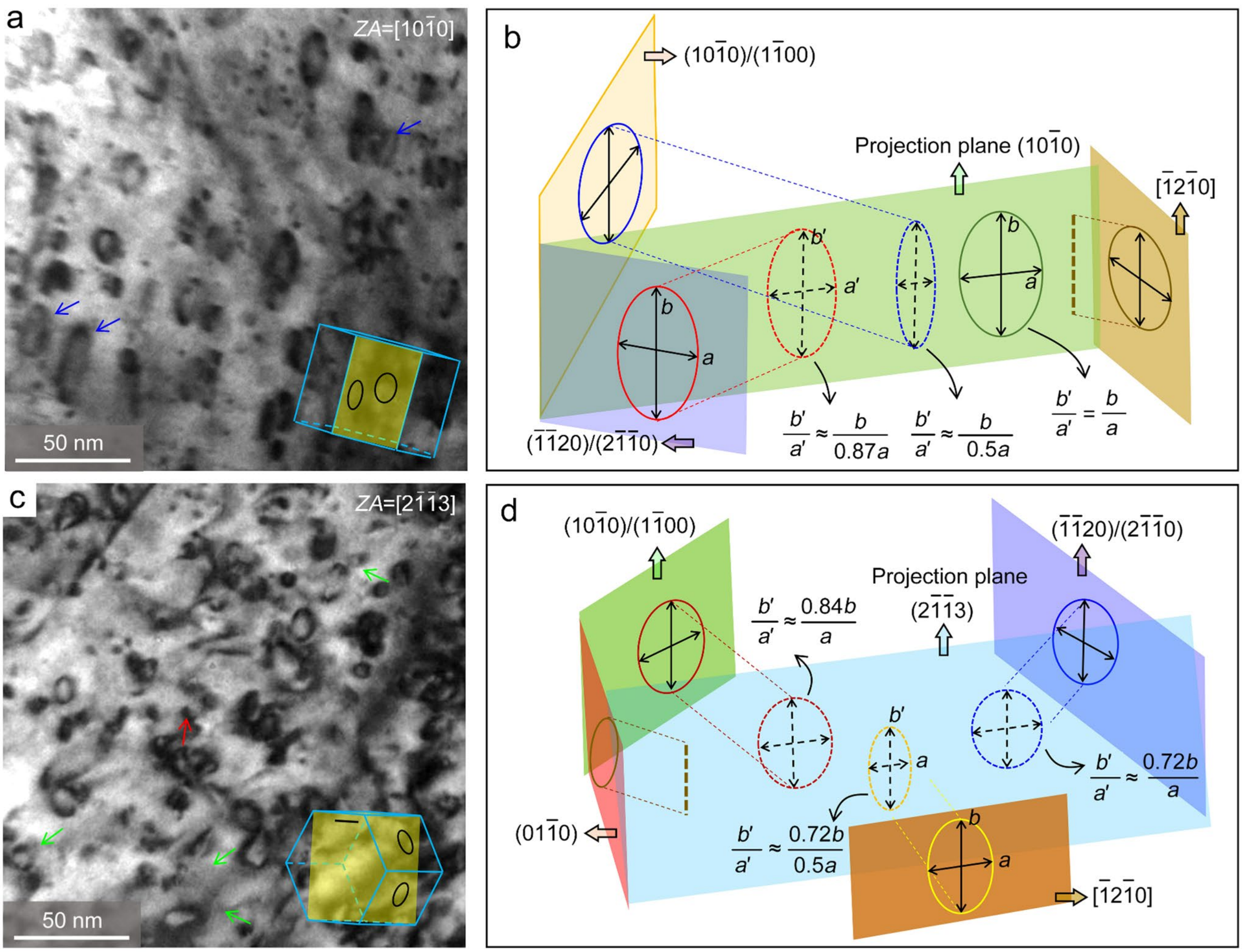

Fig. 4 Morphologies of the projection of the ⟨a⟩ loops. **a** An elliptical shape of the most ⟨a⟩ loops under viewing direction of $[10\bar{1}0]$. **b** Schematic showing the morphology of ⟨a⟩ loops on the various habit planes and their projection on the $(10\bar{1}0)$. **c** A near circular shape ⟨a⟩ loops with axis of $[2\bar{1}\bar{1}3]$. **d** Schematic of projection of ⟨a⟩ loops from $\{10\bar{1}0\}$ and $\{2\bar{1}\bar{1}0\}$ onto the plane $(2\bar{1}\bar{1}3)$. The solid lines in **b** and **d** represent the real position of ⟨a⟩ loops and the dashed lines represent the projected shape of the loops. *a* represents the minor axis of the dislocation loop, and *b* represents the major axis, which are parallel to the basal plane and *c*-axis, respectively

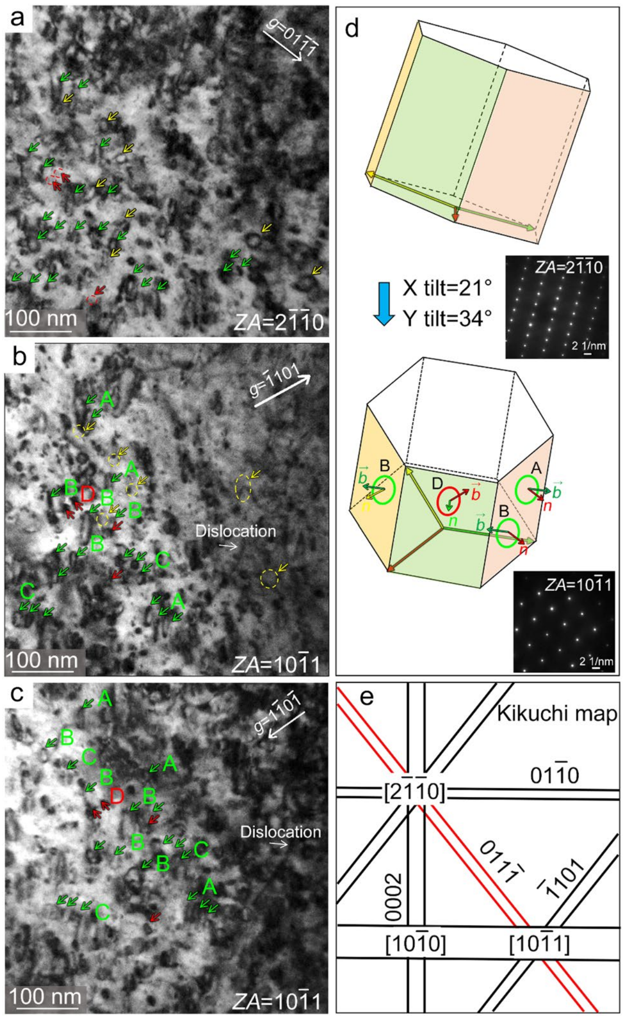

Fig. 5 Determination of the nature of $\langle a \rangle$ loops in pure Zr after helium irradiation to a fluence of 1×10^{17} ions·cm^{-2} at 400 °C. **a** Loops marked with red arrows showing no contrast under $\vec{g} = [01\bar{1}\bar{1}]$ and ZA $= [10\bar{1}1]$; **b** Loops labeled with yellow arrows showing no contrast under $\vec{g} = [\bar{1}101]$ and ZA $= [10\bar{1}1]$; **c** Bright-filed TEM image under $\vec{g} = [1\bar{1}0\bar{1}]$ and ZA $= [10\bar{1}1]$. **d** Schematic HCP unit cell and their diffraction patterns in **a** and **b**. **e** Simplified diagram of the Kikuchi map showing the zone axis tilting from $[2\bar{1}\bar{1}0]$ to $[10\bar{1}1]$ along the $(01\bar{1}\bar{1})$ Kikuchi line

elliptical shape because of the crystal anisotropy, the length of the minor axis of $\langle a \rangle$ loops was measured from [0001] zone axis. Totally 233 dislocation loops in the area of 1.6×10^{-13} m^2 were obtained for the foil with 0.5 dpa, and thus the average size of $\langle a \rangle$ loops in this region was 10.4 nm. In the case of foil with damage of 1.5 dpa, 183 dislocation loops were measured and the average size was 7.8 nm. The size distribution of the dislocation loops was plotted in Fig. 6f.

7 Number density of dislocation loops

The number density of $\langle a \rangle$ dislocation loops was counted in a TEM foil, considering the surface effect [34]. No loops were observed at the edge of the thin foil in this work because the sample thickness in this region is only 60 nm. The diameter of interstitial loops near the surface is smaller than that in the center of the foil because of the fast movement of interstitials toward the sample surface [35]. We found only when the foil thickness is thicker than 100 nm, the sample has sufficient dislocation loops and the surface sink effect is negligible [34]. For TEM foil with a thickness higher than 150 nm, many dislocation loops are likely to stack over together, and their contrast is weak, which would cause difficulty in analysis and measurement. Therefore, a TEM foil with thickness in the range of 100–150 nm is the right condition for detailed dislocation loop characterization (Fig. 7a). Weak-beam dark-field (WBDF) images have previously been used to study the geometry and structural information of loops with sizes larger than 10 nm [26]. Because of its better contrast, WBDF was used to image the $\langle a \rangle$ dislocation loops. Figure 7b shows the small-sized dislocation loops and dislocation lines with strong bright contrast, compared with the conventional dark-field image in Fig. 7c. Thus the $\langle a \rangle$ dislocation loops can be easily counted. The density of dislocation loops in the samples with irradiation damage of 0.5 dpa and 1.5 dpa is 2.26×10^{24} m^{-3} and 4.5×10^{24} m^{-3}, respectively. The results are similar to dislocation loop density measured by X-ray line profile analysis [5, 13, 36].

8 Defects on basal plane

A few $\langle c \rangle$ loops were observed in pure Zr with irradiation damage of 1.5 dpa (Fig. 8). $\langle c \rangle$ loops have line contrast when viewed along $\langle \bar{1}2\bar{1}0 \rangle$ and $\langle 10\bar{1}0 \rangle$ zone axis under $\vec{g} = [0002]$; their sizes range from 40 to 50 nm. When viewing along the [0001] zone axis, it is hard to separate $\langle a \rangle$ loops and $\langle c \rangle$ loops because of a strong stress field interference, as shown in Fig. 8b. From the dark field with $\vec{g} = [\bar{1}2\bar{1}0]$ in Fig. 8c, two white circles indicated by the yellow arrows are $\langle c \rangle$ loops, with Burgers vector of $\frac{1}{6}[2\bar{2}03]$ or $\frac{1}{6}[02\bar{2}3]$. No further determination of vacancy or interstitial type is conducted because of the foil quality. Apart from loops, a large number of triangular-vacancy platelets (TVPs) were also observed on the basal plane with an under-focus imaging condition, as indicated by the yellow arrows in Fig. 9a, b. The vacancy properties can be determined according to Fresnel fringes [3], with an under focused imaging condition, most of vacancy defects have

Table 3 Characteristics of $\langle a \rangle$ dislocation loops formed in pure Zr after helium irradiation to 0.5 dpa in Fig. 5

Number	Contrast for $\vec{g} = \bar{1}101$	Burgers vector	Habit plane	Type in nature
A	Outside	$\frac{1}{3}[\bar{1}2\bar{1}0]$	$0\bar{1}10$	Interstitial
B	Inside	$-\frac{1}{3}[\bar{1}2\bar{1}0]$	$01\bar{1}0$	Vacancy
C	Inside	$-\frac{1}{3}[\bar{1}2\bar{1}0]$	$1\bar{1}00$	Interstitial
D	Outside	$-\frac{1}{3}[2\bar{1}\bar{1}0]$	$1\bar{1}00/10\bar{1}0$	Vacancy

a white contrast. These defects were considered to be the precursor of $\langle c \rangle$ loops [3]. The density of TVPs was calculated using the area of TVPs divided by the volume of the observed region. It is clear that the density of TVPs increase with the radiation damage, indicating the gradual accumulation of point defects.

9 Irradiation dose-dependent defect characteristics

Our studies focus on the characteristic of interstitial and vacancy defects in pure Zr in the early stage of the irradiation with 0.5 dpa and 1.5 dpa. All the defects size distribution and number density were concluded in Table 4. With the irradiation dose increasing, no significant changes of the $\langle a \rangle$ loop density were observed, which indicate that the number of dislocation loops reached a saturation immediately. The average size of the dislocation loops decreases slightly (Fig. 6c). The ratio of vacancy loops to interstitial loops

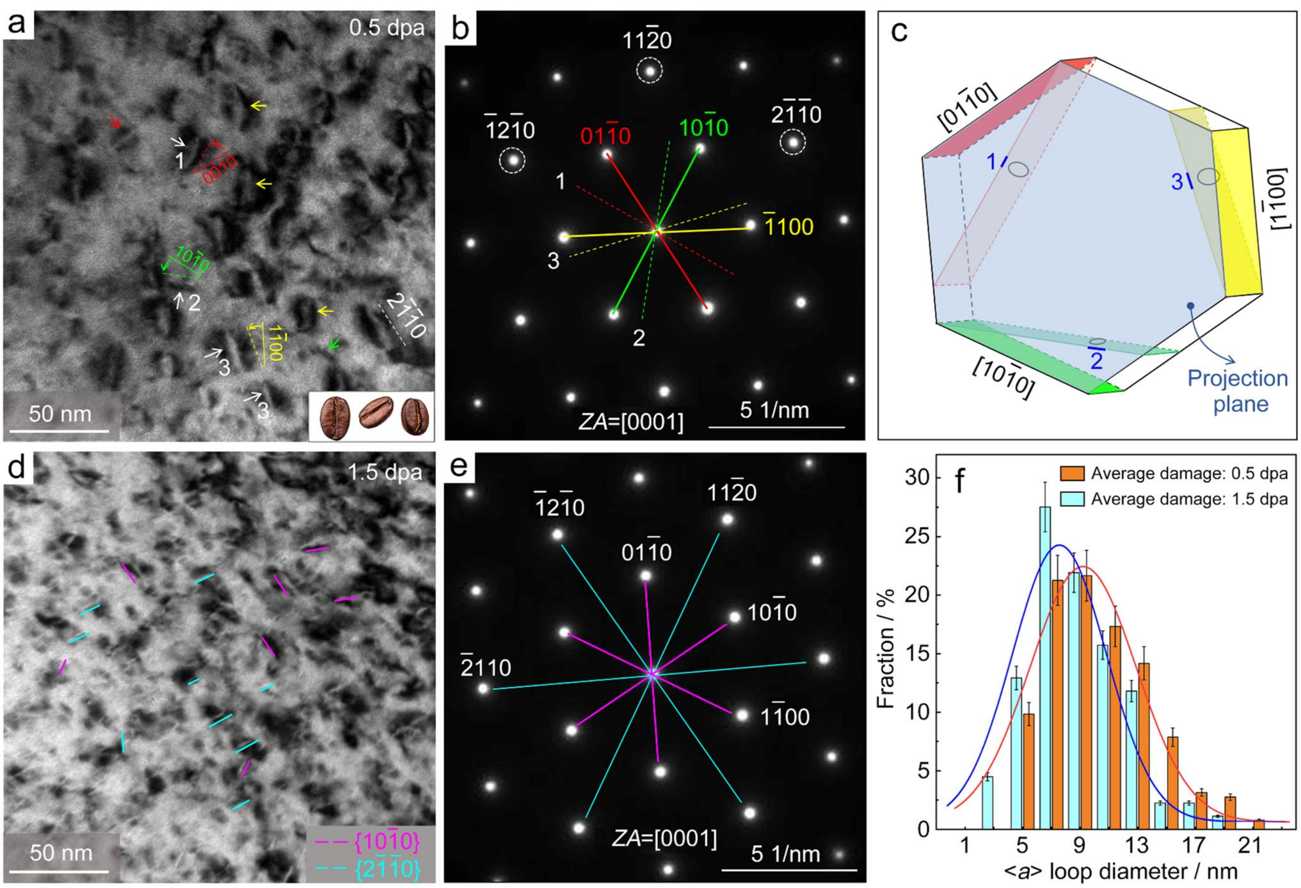

Fig. 6 Morphologies of $\langle a \rangle$ dislocation loops under viewing axis of [0001]. **a** $\langle a \rangle$ loops with a "coffee bean" contrast after helium irradiation to 0.5 dpa. The inserted image illustrates the shape of the coffee beans. The three dashed lines in **b** represent the habit plane of Nos. 1, 2 and 3 loops. The habit plane of Nos. 1–3 loops rotates from the primary prismatic plane to the secondary prismatic plane. **c** Schematic showing the viewing direction and the projection of $\langle a \rangle$ loops on the basal plane. Loops with dashed line are the real loops and the solid lines are the projected loops. **d** The formation of the smaller and denser $\langle a \rangle$ loops with increasing of average irradiation damage to 1.5 dpa. Blue lines mark $\langle a \rangle$ loops lying near the $\{11\bar{2}0\}$ plane and pink lines indicate those on the $\{10\bar{1}0\}$ plane. **e** Diffraction pattern of the irradiated-Zr in **d**. **f** Size distribution of $\langle a \rangle$ with average irradiation damage of 0.5 dpa and 1.5 dpa. 233 loops for 0.5 dpa and 183 loops for 1.5 dpa were involved in the statistics. The difference in foil thickness between **a** and **d** is less than that 20 nm

changes from 1.3 (0.5 dpa) to 1.1 (1.5 dpa), which shows that the number of vacancy-type $\langle a \rangle$ loops decreases slightly as radiation damage increases.

The cascade induced point defects annihilate at the sinks or form into dislocation loops. The density of $\langle a \rangle$ loops reaches saturation quickly at a lower radiation damage (0.2 dpa) [15–19]. As more and more point defects are introduced into the foils, the existing dislocation loops served as sinks for interstitials and vacancies. Compared with a vacancy, dislocation loops prefer to capture interstitial atoms [18, 37]. With the absorption of interstitials, interstitial loops grow and the vacancy loops shrink. Vacancies prefer to be absorbed by a former formed vacancy loop on the prismatic plane or accumulate on the basal plane to evolve into $\langle c \rangle$ loops. However, the number of vacancies required to enlarge $\langle a \rangle$ loops is much more than that for a $\langle c \rangle$ loop [38]. In addition, the vacancies diffuse slower along the $\langle a \rangle$ direction than that along $\langle c \rangle$ direction [39]. Thus, excess vacancies are more likely to gather on the basal plane to form vacancy-type defects (like TVPs) rather than to be absorbed by an already formed vacancy $\langle a \rangle$ loop, as shown in Fig. 9. The formed $\langle a \rangle$ interstitial loops and their collapse cause expansion along a-direction, which is the opposite of vacancy loops. At the initial stage of irradiation, the earlier formation of interstitial $\langle a \rangle$ loops cause a fast growth rate along a-direction, corresponding to the rapid irradiation growth. The appearance of

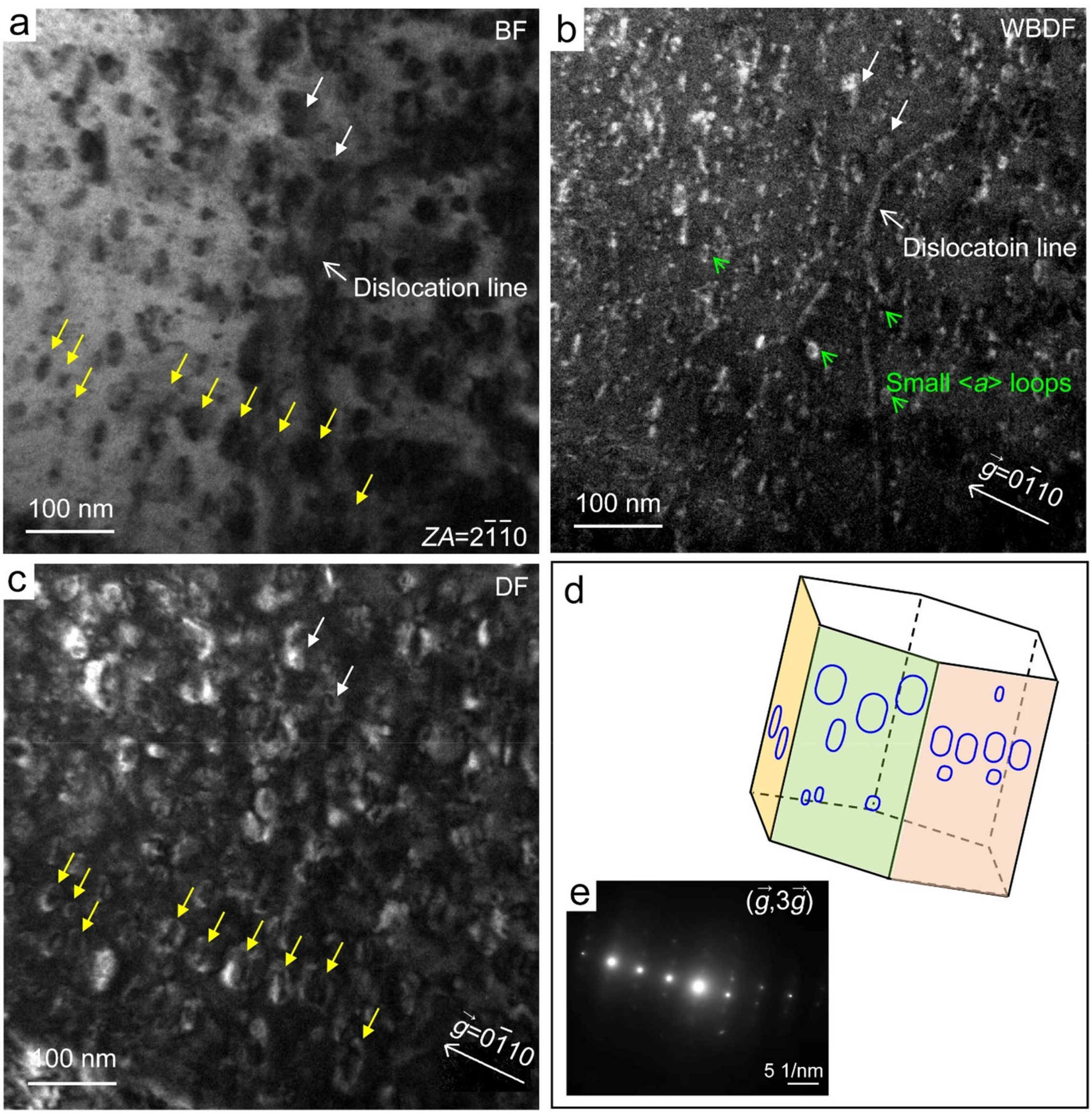

Fig. 7 Queue of $\langle a \rangle$ loops. **a** Bright-field and **b** WBDF image (***g***,3 ***g***) of $\langle a \rangle$ loops with $\vec{g}=[0\bar{1}10]$. **c** Dark-field TEM image of $\langle a \rangle$ loops arranged in a row along the basal plane, in the same position as in **b**. The thickness of sample in this region (130 ± 10 nm). **d** Schematic showing the queue of $\langle a \rangle$ loops in these regions. **e** Diffraction pattern of WBDF image in **b**

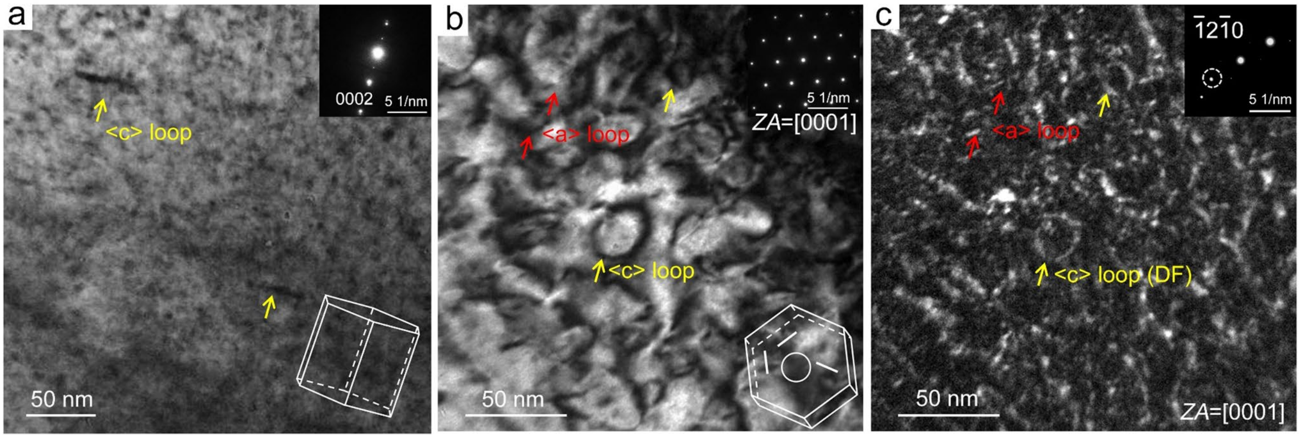

Fig. 8 Morphologies of $\langle c \rangle$ loops under *a*-axis and *c*-axis. **a** $\langle c \rangle$ loops with a line contrast parallel to the basal plane under viewing direction of a-axis. **b** $\langle c \rangle$ loops with a near spherical shape on the basal plane with viewing direction of c-axis. **c** Dark-field TEM image of $\langle c \rangle$ loops with a circular shape. The image was taken under double beam condition with $\vec{g} = [2\bar{1}\bar{1}0]$

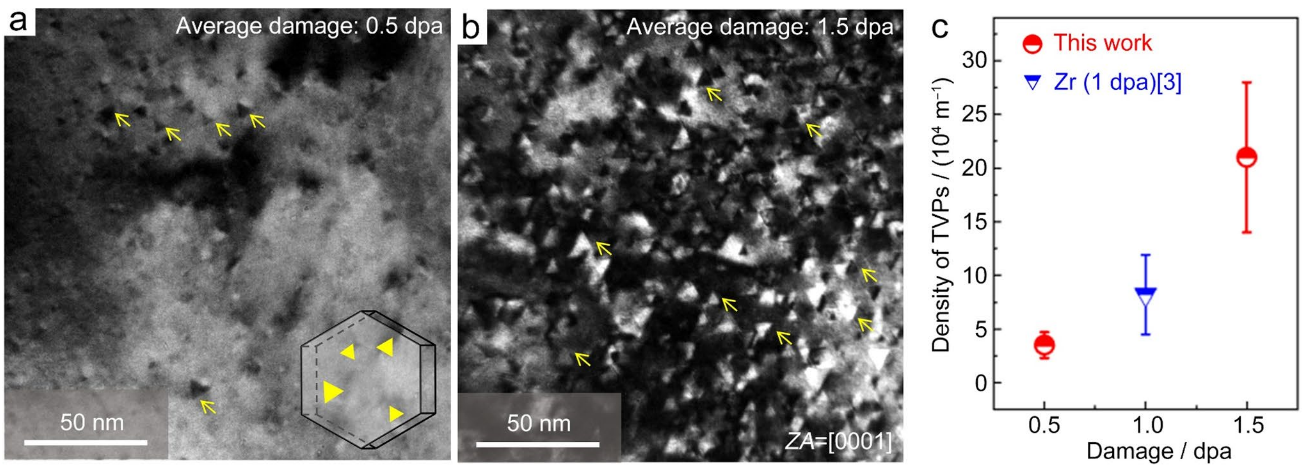

Fig. 9 Vacancy type defects on the basal plane. **a**, **b** Triangle-shaped vacancy platelets produced after helium irradiation to different dose level. **c** The increasing number density of triangle-shaped vacancy platelets with irradiation damage from 0.5 to 1.5 dpa [3]

Table 4 Size distribution and number density of a-loop, c-loop and TVP

Defects	a-loop		c-loop		TVP	
Damage (dpa)	0.5	1.5	0.5	1.5	0.5	1.5
Size distribution (nm)	2–30	3–18	–	40–50	2–12	3–13
Average size (nm)	10.4	7.8	–	43	4.6	6.6
Number density (m^{-3})	2.26×10^{24}	4.5×10^{24}	–	5×10^{20}	2.5×10^{21}	6.8×10^{21}
Area density (m^{-1})	–				4.74×10^{4}	2.1×10^{5}

vacancy loops alleviates this phenomenon. With increasing irradiation damage, the total number density of dislocation loops remains constant because interstitial atoms are likely consumed by the existing vacancy loops, reaching a steady state. The density of TVPs increases exponentially with irradiation dose (Fig. 9c), which could cause a significant contraction along the *c*-axis. The evolution of these defects with irradiation damage is consistent with the second stage of irradiation growth [4, 17].

10 Conclusions

In summary, we performed detailed characterization and analysis on the dislocation loops in helium irradiated pure Zr TEM foil. Via such an example, our aim was to show a simple procedure to analyze dislocation loops in an HCP crystal. The habit plane of $\langle a \rangle$ loops was determined by tilting the sample to different zone axis and judging based on their projection aspect ratio. The dislocation loop size can be easily measured from [0001] direction. The number density of dislocation loops can be accurately counted under a WBDF imaging condition. With increasing the irradiation dose, the density of $\langle a \rangle$ dislocation loops kept constant, while a few $\langle c \rangle$ loops formed on the basal plane in addition to a high number density of TVPs. The variation of vacancy-type defects with increasing irradiation dose agrees well with the irradiation growth curve.

Acknowledgements This work was financially supported by the National Natural Science Foundation of China (Grant Nos. 51922082 and 51971170) and the 111 Project of China (Grant No. BP2018008).

Author contributions Si-Mian Liu performed the experiments under the guidance of Wei-Zhong Han; all authors discussed and contributed to the writing and revisions.

Declarations

Conflict of interest The authors declare no conflict of interest.

References

1. Gulden TD, Bernstein IM. Dislocation loops in irradiated zirconium. Philos Mag. 1966;14:1087.
2. Maker DM, Eyre BL. Characterization of small perfect dislocation loops by transmission electron microscopy. Philos Mag. 1972;26:1233.
3. Liu SM, Beyerlein IJ, Han WZ. Two-dimensional vacancy platelets as precursors for basal dislocation loops in hexagonal zirconium. Nat Commun. 2020;11:5766.
4. Northwood DO, Fidleris V, Gilbert RW, Carpenter GJC. Dislocation loop generation and irradiation growth in a zirconium single crystal. J Nucl Mater. 1976;61:123.
5. Yang HL, Kano S, McGrady J, Chen DY, Murakami K, Abe H. Microstructural evolution and hardening effect in low-dose self-ion irradiated Zr–Nb alloys. J Nucl Mater. 2020;542:152523.
6. Topping M, Harte A, Ungár T, Race CP, Dumbill S, Frankel P, Preuss M. The effect of irradiation temperature on damage structures in proton-irradiated zirconium alloys. J Nucl Mater. 2019;514:358.
7. Griffiths M, Loretto MH, Smallman RE. Anisotropic distribution of dislocation loops in HVEM-irradiated Zr. Philos Mag A. 1984;49:613.
8. Jostsons A, Kelly PM, Blake RG. The nature of dislocation loops in neytron irradiated zirconium. J Nucl Mater. 1977;66:236.
9. Kelly PM, Blake RG. The characterization of dislocation loops in neutron irradiated zirconium. Philos Mag. 1973;28(2):415.
10. Carpenter GJC, Watter JF. A study of electron irradiation damage in zirconium using a HVEM. J Nucl Mater. 1982;96:213.
11. Griffiths M, Loretto MH, Smallman RE. Electron damage in zirconium-I. Defect structure and loop character. J Nucl Mater. 1983;115:313.
12. Zu XT, Sun K, Atzmon M, Wang LM, You LP, Wan FR, Busby JT, Was GS, Adamson RB. Effect of proton and Ne irradiation on the microstructure of Zircaloy 4. Philos Mag. 2006;85:649.
13. Idrees Y, Yao Z, Kirk MA, Daymond MR. In situ study of defect accumulation in zirconium under heavy ion irradiation. J Nucl Mater. 2013;433:95.
14. Zhang JW, Liu SM, Han WZ. Interfaces reduce dislocation loop formation in irradiated nanolayered Zr-2.5Nb. Scripta Mater. 2021;200:113902.
15. Griffiths M, Loretto MH, Smallman RE. Electron damage in zirconiumII. Nucleation and growth of c-component loops. J Nucl Mater. 1983;115:323.
16. Adamson RB, Coleman CE, Griffiths M. Irradiation creep and growth of zirconium alloys: a critical review. J Nucl Mater. 2019;521:167.
17. Rogerson A. Irradiation growth in zirconium growth in zirconium and its alloys. J Nucl Mater. 1988;159:43.
18. Bacon DJ. Point defects and clusters in the HCP metals: their role in the dose transition. J Nucl Mater. 1993;206:249.
19. Li Y, Ghoniem N. Cluster dynamics modeling of irradiation growth in single crystal Zr. J Nucl Mater. 2020;540:152312.
20. Francis E, Babu RP, Harte A, Martin TL, Frankel P, Jädernäs D, Romero J, Hallstadius L, Bagot PAJ, Moody MP, Preuss M. Effect of Nb and Fe on damage evolution in a Zr-alloy during proton and neutron irradiation. Acta Mater. 2019;165:603.
21. Cockeram BV, Leonard KJ, Byun TS, Snead LL, Hollenbeck JL. Development of microstructure and irradiation hardening of Zircaloy during low dose neutron irradiation at nominally 377–440 °C. J Nucl Mater. 2014;449:69.
22. Yao ZW, Daymond M, Di S, Idrees Y. Irradiation induced defect clustering in zircaloy-2. Appl Sci. 2017;7:854.
23. Yu H, Yao Z, Idrees Y, Zhang HK, Kirk MA, Daymond MR. Accumulation of dislocation loops in the α phase of Zr Excel alloy under heavy ion irradiation. J Nucl Mater. 2017;491:232.
24. Naceri SE, Izerrouken M, Sari A, Ryelandt S, Menchi O, Ghamnia M. Effect of 165-keV Ar-ion irradiation on microstructural and mechanical properties of zircaloy-4. J Radioanal Nucl Chem. 2020;323(2):817.
25. Groves GW, Kelly A. Interstitial dislocation loops in magnesium oxide. Philos Mag. 1961;6:1527.
26. Jenkins ML. Characterisation of radiation-damage microstructures by TEM. J Nucl Mater. 1994;216:124.
27. Maher DM, Eyre BL. Neutron irradiation damage in molybdenum. Philos Mag. 1971;23:409.
28. Foll H, Wilkens M. A simple method for the analysis of dislocation loops by means of the inside-outside contrast on transmission electron micrograph. Phys Stat Sol. 1975;31:519.
29. Carpenter GJC. Unsafe orientations for the characterisation of dislocation. Phys Stat Sol. 1976;37:K61.
30. Yang TS, Yu GP, Chen LJ. The Characterization of nitrogen-ion-irradiation induced dislocation loops in zirconium. Phys Stat Sol. 1985;92:399.
31. Stoller RE, Toloczko MB, Was GS, Certain AG, Dwaraknath S, Garner FA. On the use of SRIM for computing radiation damage exposure. Nucl Instrum Methods Phys Res B. 2013;310:75.
32. Hulse R, Race CP. An atomistic modelling study of the properties of dislocation loops in zirconium. J Nucl Mater. 2021;546:152752.
33. Buckley SN, Bullough R, Hayns MR. The direct observation of irradiation damage in zirconium and its alloys. J Nucl Mater. 1980;89:283.

34. Xu D, Wirth BD, Li M, Kirk MA. Combining in situ transmission electron microscopy irradiation experiments with cluster dynamics modeling to study nanoscale defect agglomeration in structural metals. Acta Mater. 2012;60:4286.
35. Woo CH, Liu X. Atomistic calculation of point-defect diffusion anisotropy and irradiation growth in α-zirconium. Philos Mag. 2007;87:2355.
36. Ungár T, Frankel P, Ribárik G, Race CP, Preuss M. Size-distribution of irradiation-induced dislocation-loops in materials used in the nuclear industry. J Nucl Mater. 2021;550:152945.
37. Woo CH. Dislocation bias in an anisotropic diffusion medium and irradiation growth. J Nucl Mater. 1983;119:219.
38. Christensen M, Wolf W, Freeman C, Wimmer E, Adamson RB, Griffiths M, Mader EV. Vacancy loops in breakaway irradiation growth of zirconium: Insight from atomistic simulations. J Nucl Mater. 2020;529:151946.
39. Christensen M, Wolf W, Freeman C, Wimmer E, Adamson RB, Hallstadius L, Cantonwine PE, Mader EV. Diffusion of point defects, nucleation of dislocation loops, and effect of hydrogen in hcp-Zr: Ab initio and classical simulations. J Nucl Mater. 2015;460:82.

Dr. Wei-Zhong Han currently works in CAMP-Nano of the School of Materials Science and Engineering, Xi'an Jiaotong University. He received Ph.D degree from the Institute of Metal Research, Chinese Academy of Sciences in 2008. Before joining in Xi'an Jiaotong University, he worked as a research fellow at ARC Centre of Excellence for Design in Light Metals in Monash University for two years and at the Center for Materials at Irradiation and Mechanical Extremes, Los Alamos National Laboratory for three years. Prof. Han's research focuses on the mechanical and irradiation damage mechanisms of metallic materials; Interface and defect engineering in metals and alloys.